PRE-TEST OF A LIGHT-WEIGHT CFRP WING SEGMENT OF A HIGH ALTITUDE PLATFORM FOR IN-FLIGHT LOAD MEASUREMENTS BASED ON STRAINS

Arne Voß, Keith Soal, Julian Sinske, David Meier, DLR - German Aerospace Center, Institute of Aeroelasticity, Göttingen, Germany

Steffen Niemann, Jörg Nickel, Michael Hanke, DLR - German Aerospace Center, Institute of Composite Structures and Adaptive Systems, Braunschweig, Germany

Abstract

For the validation of loads and aeroelastic simulations of a high altitude platform (HAP) in-flight, load measurements are very helpful. One technique to obtain load measurements is to apply strain gages to the primary structure. A calibration procedure enables the reconstruction of the loads from the measured strains. To reduce the risks, gain confidence and establish a feasible measurement set-up, a pre-test based on a CFRP wing segment is performed. This paper presents the theoretical background and the set-up of the measurement equipment. The results of the calibration from three different test cases are presented, showing an excellent agreement between applied and reconstructed loading with a deviation of $\leq \pm 1.0N$ and $\leq \pm 2.0cm$ for the location. Finally, the strains measured in the experiment are compared with the simulation, showing that a prediction of the strains is possible within a range of $\leq \pm 8\%$.

Keywords

High Altitude Platform, flight test, load measurement, strain gages, strains

1. MOTIVATION AND INTRODUCTION

The DLR is currently developing the high altitude, long endurance, solar electric aircraft HAP that can serve as a platform for scientists to make observations of the earth over a long period of time.

The loads and aeroelastic properties of that configuration are investigated in detail [8,9]. For the validation of the numerical simulations, load measurements taken during flight testing are very helpful. A typical example for a load quantity of interest could be e.g. the shear force F_z, the bending moment M_x and the torsional moment M_y at the wing root. However, to the best of the authors knowledge, there are no means to measure section loads directly.

One technique to obtain information on loads, is to apply strain gages to the primary structure of an aircraft at the locations of interest. Then, selected forces are applied to the structure in a ground test and the strains are recorded. Because both the strains and forces are known, a calibration matrix β (or Skopinski-Matrix) can be calculated that establishes the relation between loads and strains. During the flight test, the strains are recorded and by application of the calibration matrix, the loads that must have acted of the aircraft can be reconstructed in a post-processing step.

The basic principles were first described by Skopinski et al. [7] in 1954. Since then, only a few publications are available. Two comprehensive reports were published by Eckstrom [1] and Jenkins and DeAngelis [2]. A more recent publication, but with restricted access (LTH), is published by Schmücker [5]. The DLR itself has some experiences at the example the sailplane Discus 2c [4], an under-wing carrier of the Gulfstream G550 “HALO” [6], and is currently preparing to equip the Dassault Falcon 2000LX “ISTAR” [11]. For the Discus 2c, time domain simulations showed a very good agreement of the dynamic loads with the measurements [10].

Difficulties encountered during the calibration process will potentially lead to a delay of the flight test or a flight test without proper load measurements. To reduce the risks and to gain confidence in establishing a feasible measurement set-up specific to the HAP aircraft, a pre-test based on a wing segment is planned. The following questions shall be investigated:

1. Is it possible to transfer the measurement set-up (from the well-documented wing box structure) to a structure with a single tube-spar and which strain gage locations should be used?
2. Which load cases should be used for the calibration and how many load cases are necessary?

3. Comparison of the measured and simulated strains. How well can the measurements be predicted?
4. Is it possible to isolate the strain gages against surface temperature fluctuations?

2. THEORETICAL BACKGROUND

This section presents a short summary of the mathematical operations involved in the Skopinski method. The more details and the derivation is given by Skopinski [7].

A linear relationship between the strain μ_1 and the shear force F_z, the bending moment M_x and the torsional moment M_y can be expressed as

(2.1) $$\mu_1 = \alpha_{11} \cdot F_z + \alpha_{12} \cdot M_x + \alpha_{13} \cdot M_y$$

using coefficients α. For strains measured at multiple locations, the above equation is cast into matrix notation

(2.2) $$\boldsymbol{\mu} = \boldsymbol{\alpha} \cdot \mathbf{v}$$

with the load vector $\mathbf{v}$, coefficient matrix $\boldsymbol{\alpha}$ and strain vector $\boldsymbol{\mu}$. The inverse $\boldsymbol{\beta} = \boldsymbol{\alpha}^{-1}$ leads to the calibration matrix (or Skopinski-Matrix) $\boldsymbol{\beta}$ and allows to calculate loads $\mathbf{v}$

(2.3) $$\mathbf{v} = \boldsymbol{\beta} \cdot \boldsymbol{\mu}$$

based on strains $\boldsymbol{\mu}$ as input. Because the system is undetermined in most cases, finding $\boldsymbol{\beta}$ involves solving a system of equations

(2.4) $$\boldsymbol{\beta} = \mathbf{v} \cdot \boldsymbol{\mu}^T \cdot \left[\boldsymbol{\mu} \cdot \boldsymbol{\mu}^T\right]^{-1}$$

in a least squares sense. Note that the input vector $\boldsymbol{\mu}$ may be strains, but using other inputs such as the measurement bridge response in milli- or micro-volt is possible, too. Finally, Skopinski et al. suggest to calculate a probable error p.e. for the loads

(2.5) $$p.e. = 0.6745 \cdot \sqrt{\frac{\sum \epsilon^2}{n - (q+1)}}$$

with the number of load cases n, the number of calibration coefficients q and the residual ϵ.

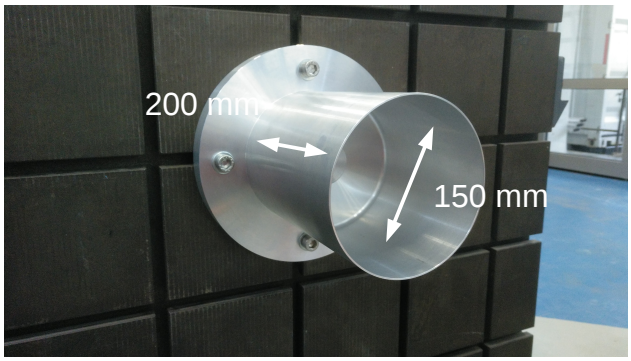

Figure 1: Aluminum mounting for the wing root

3. TEST SECTION AND SET-UP OF MEASUREMENT EQUIPMENT

3.1. Description of Test Body

The test section, see Figure 2, is a wing section with a length of 3.0 m taken from the preliminary design of the HAP configuration. The wing consists of a tube with an inner diameter of 150.0 mm as main spar. The tube is made from carbon fiber material and the fibers are wound around a cone at an angle of 20° plus additional plies at an angle of 90°, leading to a material thickness of 0.87 mm. Both the material properties and thicknesses are representative for a mid-wing section of the HAP configuration.

Four ribs are added to the outer section of the wing segment with a spacing of 400.0 mm. The rips are cut from a carbon fiber sandwich plate with a thickness of 4.0 mm. Again, both the material and spacing are representative for the final aircraft. For the purpose of the test, a more simple and more practical rib design was selected. The ribs are slightly shorter (1.10 m instead of 1.49 m), thus

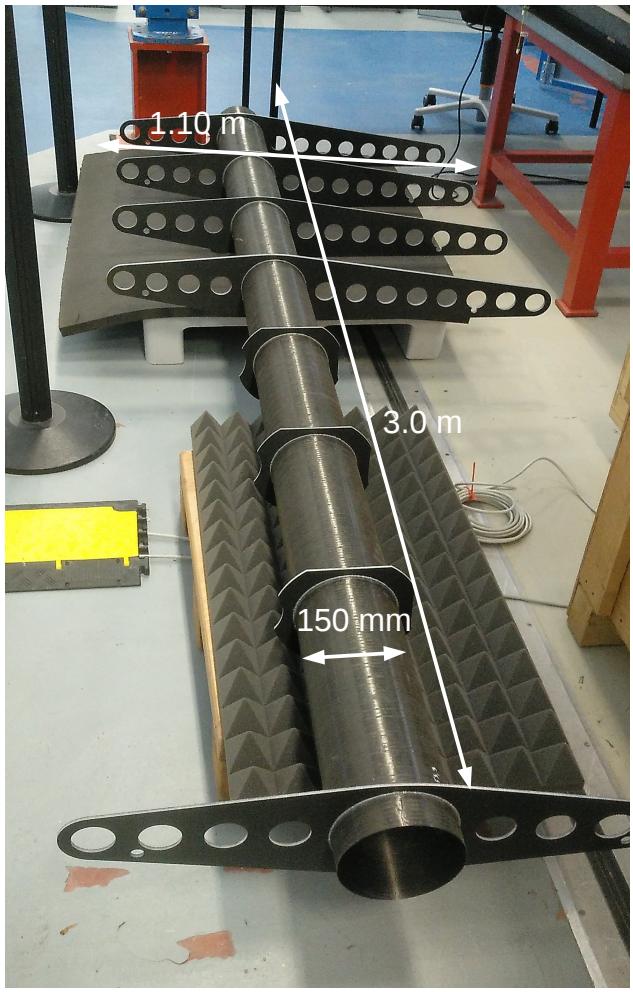

Figure 2: Test section representative for the mid-wing of the HAP configuration

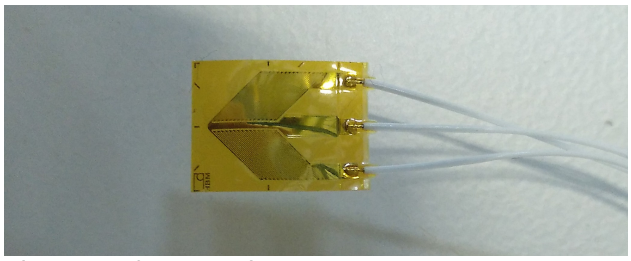

Figure 3: +/- 45° strain gage, type HBM K-CXY4-006-1-350-020

being more robust, and fit into the vehicle used for the transportation from the manufacturing site (Braunschweig) to the laboratory (Göttingen). Instead of using the airfoil shape, a symmetrical layout was chosen and holes with a diameter of 50.0 mm were added to allow for an easy introduction of the nodal loads using straps with a width of 30.0 mm.

With respect to the final wing design, only the leading and trailing edges as well as the upper and lower foil skin are missing. For the first two, the design is not yet finalized and the foil skin would prevent an easy access to the primary structure to attach loads. Their influence is considered to be small and negligible for the purpose of this test.

The wing is mounted at the wing root to a vertical machine bed, which in turn is attached to a 1.5 t metal cube. For the design of the mounting, the aim was to

- provide a large area for gluing and
- to avoid an abrupt jump in the material characteristics (and thus in the stress and strain distribution) between clamping and tube.

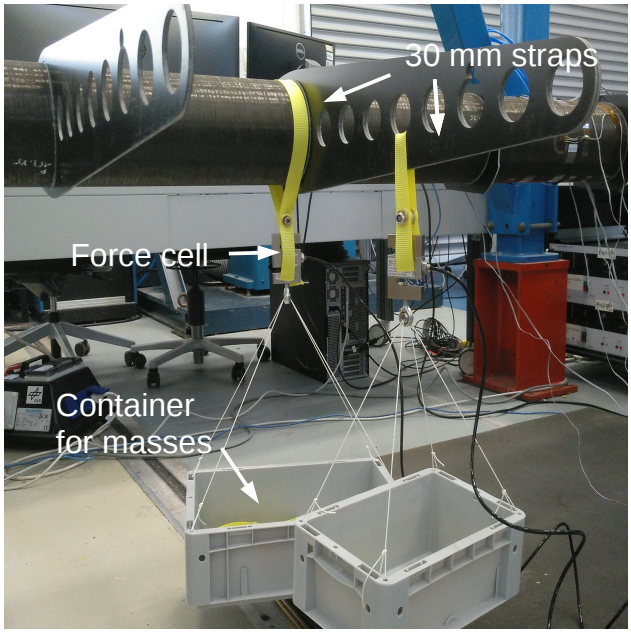

Figure 4: Set-up to apply nodal loads to the structure at different locations

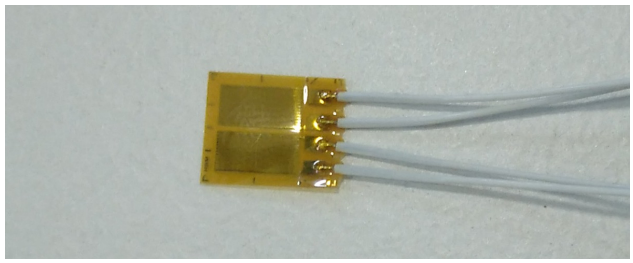

Figure 5: Double linear strain gage, type HBM K-CDY4-0060-1-350-020-N

The resulting attachment is shown in Figure 1. It is turned from aluminum, has a length of 200.0 mm and a material thickness of 1.5 mm. In this way, it is representative for the shafting that will be used for the final aircraft at the locations where two tubes are joined.

3.2. Selection of Measurement Equipment

The measurement system is an imc CRFX-2000GP-1 [12] with an UNI2-8 module. This combination provides 8 channels and can be extended by adding more modules.

For setting up the measurement bridges, two different strain gages by HBM are selected, shown in Figures 3 and 5. A measurement grid length of 6.0 mm is chosen for good handling and better heat energy radiation compared to smaller sensors, which was motivated by the carbon fiber material and the thin material thicknesses. The HBM Y-Series is for general experimental use and is rated with 10^8 load cycles at $1000\mu m/m$ but only 10^2 load cycles at $3500\mu m/m$. For the final aircraft, much higher strain levels and load cycles are expected than in the laboratory test, thus a different sensor might be considered. Using pre-wired sensors was motivated by the aim to avoid soldering directly on the carbon fiber material, as the hot temperatures are expected to weaken the structure, which is highly undesired especially in close proximity to the sensors.

To measure the nodal forces applied to the structure, two force measurement cells are used. To apply the loads to the structure, the set-up is completed by

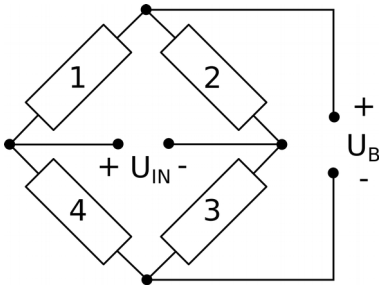

Figure 6: Layout of measurement bridge following imc naming convention

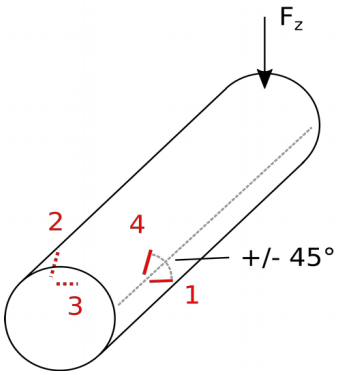

Figure 7: Shear bridge (SB) set-up

30.0 mm straps wrapped about the tube or through the holes of the ribs and attached to the upper side of the force measurement cell while masses of different size and weight are put into a plastic box attached to the lower side, as shown in Figure 4.

3.3. Measurement Bridge Layout and Installation

The full measurement bridge, see Figure 6, has a supply voltage U_B and the individual strain gages are numbered in clock-wise direction. The positive pole of the measurement voltage U_{IN} is taken between gages 1 and 4 and the negative pole is taken between 2 and 3. Thus, a stretching of gages 1 and 3 leads to a negative voltage U_{IN} and a stretching of 2 and 4 to a positive voltage U_{IN}.

With the information from above, the shear bridge (SB), see Figure 7, is set-up using two +/- 45° strain gages on the sides of the tube facing the leading and trailing edges. The wiring is such that strains due to pure torsion are compensated.

The torsion bridge (TB), see Figure 9, is similar to the shear bridge but mounted on the upper and lower side of the tube. Also, the orientation of strain gages 2 and 3 is flipped compared to the shear bridge. In this set-up, the torsion bridge is compensated against strains due to pure shear and bending.

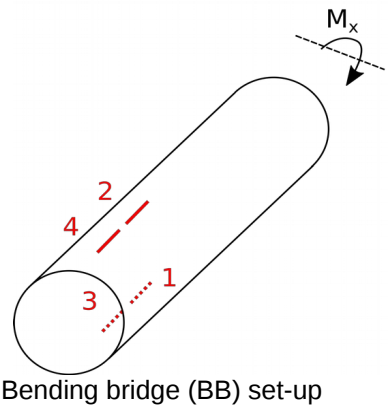

Figure 8: Bending bridge (BB) set-up

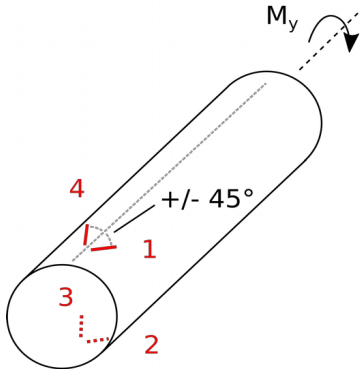

Figure 9: Torsion bridge (TB) set-up

The bending bridge (BB), see Figure 8, comprises two double linear strain gages applied to the upper and lower side of the tube. The bending bridge will not react to strains due to pure torsion.

Note that several sources and handbooks mention that full bridges are well compensated for temperature, which is only partially true. Experience has shown that there is a significant temperature drift in flight measurement data, which can be explained by the different locations of the individual sensors, for example of the upper and lower side of the wing where one sensor is exposed to the sun while the other is not. A more detailed discussion is given in section 4.4.

3.4. Load Application for Calibration

The loads are applied to the structure at different locations in chord- and span-wise direction as indicted in Figure 10. This is necessary for the decoupling of measurement bridges. For example, both the shear and bending bridge will react to a force applied to the center line, because there is no shear without bending. However, moving the same force in span-wise direction changes the bending while keeping the shear constant.

Three measurement series with single/nodal loading (B0, B1 and B2) are investigated. Measurement plan B0 is the most simple with only four locations in

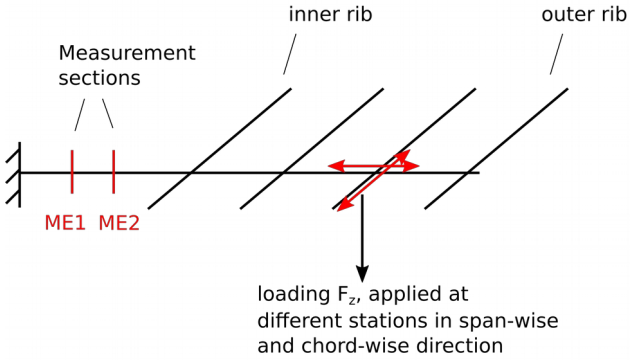

Figure 10: Overview of measurement planes ME1 and ME2 and naming convention for locations of applied forces in span- and chord-wise direction

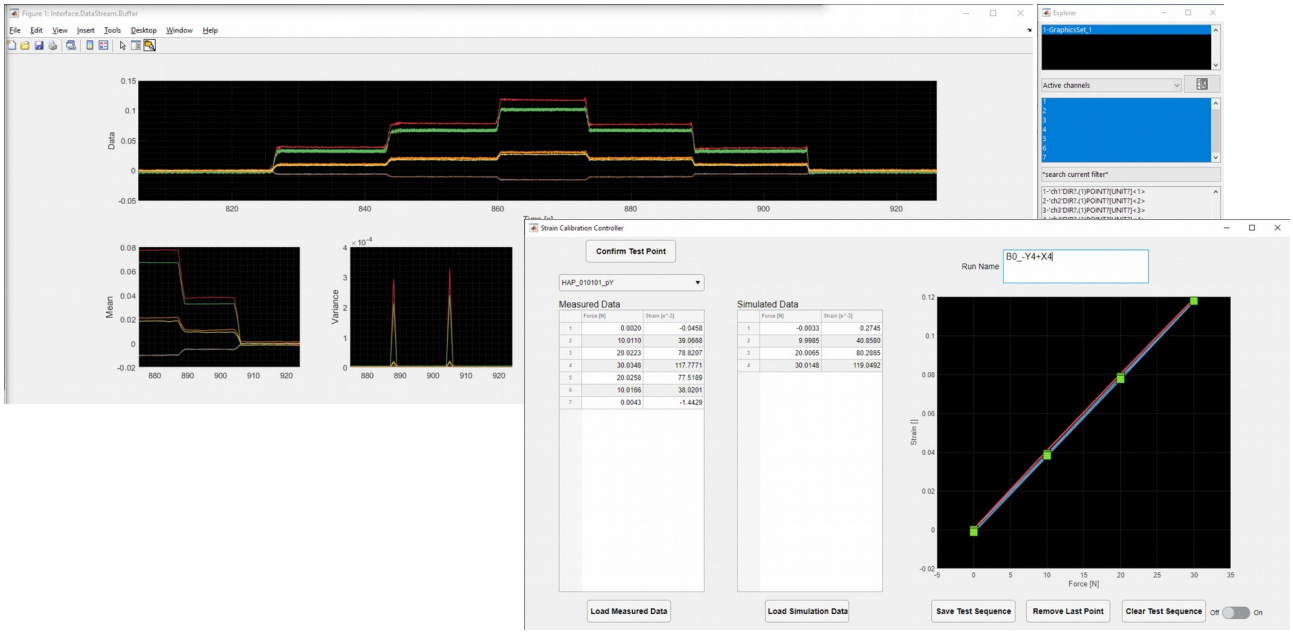

Figure 11: Custom Graphical User Interface (GUI) developed to monitor the strains online during the calibration

span-wise direction and four locations in chord-wise direction, leading to a total of 8 excitation locations. The measurement series B1 and B2 have additional, intermediate locations, leading to a total of 12 and 20 excitation locations respectively.

3.5. Online Strain Monitoring System

In order to ensure that the measured data is accurate and has a high quality it is important to observe the measured signals in real time. This serves the dual purpose of trouble shooting the test setup to identify possible mistakes in wiring or strain gage responses as well as to identify trends or undesirable effects during testing which may be difficult or impossible to resolve in post processing. An online interface to the imc measurement hardware was developed in a DLR-internal toolbox. This allows data to be received directly from the RAM of the measurement system. A custom Graphical User Interface (GUI) was developed to monitor the strain force hysteresis and to view the raw time data with interactive features. Finally during the test the user is able to capture test points, which are saved in a data class with all required meta-parameters and header information for full data traceability. A screenshot of the GUI is shown in Figure 11.

4. RESULTS AND TEST CASES

4.1. Measurement Bridge Responses

In a first step, selected responses of the measurement bridges from series B0 are presented. A negative, downward force leads to a negative response of the shear bridge 10102 and a positive response of the bending bridge 10101 in all cases.

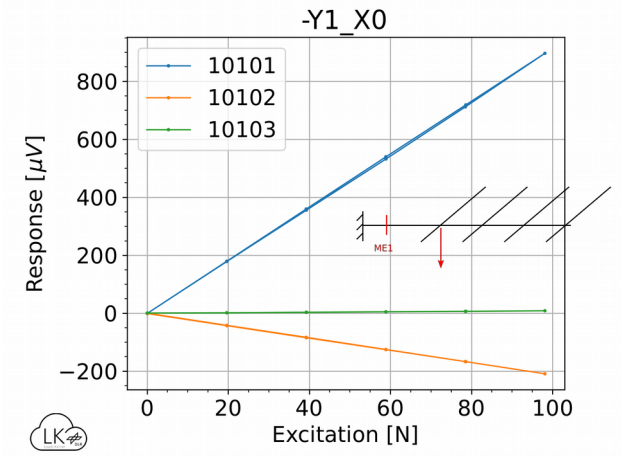

Figure 12: Excitation at the inner rib, center line

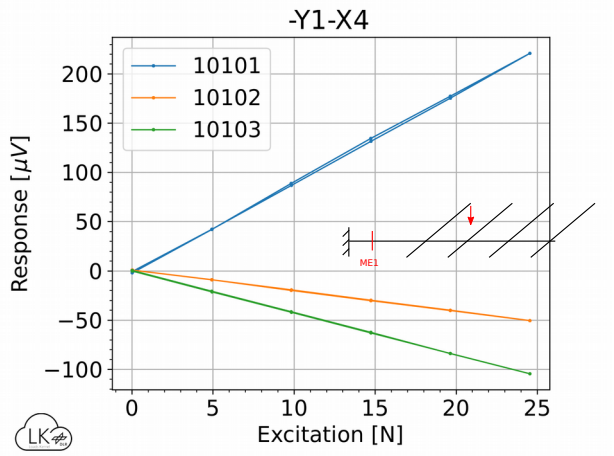

Figure 13: Excitation at the inner rib, trailing edge

Note that, for convenience, the applied force is plotted with a positive sign, although it points in a negative direction. Looking at the first excitation location at the center line of the main spar, see Figures 12, one can clearly see a distinct response of the bending bridge 10101 and the shear bridge 10102. In this case, a small response of the torsion bridge 10103 is visible, which can be explained by an imperfect installation of the bridge, presumably with a small angular misalignment. In addition, it is possible that the force application rig was positioned slightly off-center. Because of the friction between the strap and the tube's surface, it is possible to transfer small torsional loads as well. Looking at an excitation location at the leading edge, see Figure 13, the torsion bridge response 10103 is much stronger. The loading is applied in five steps and both the loading and unloading is recorded.

All bridge responses show a liner behavior. Nearly no hysteresis can be seen when loading and unloading the test body. This effect appears to be more pronounced for the cases where the force is applied to the ribs compared to an application of the forces directly to the main spar, although it has not been quantified any further.

4.2. Calculation of the Calibration Matrix

In a second step, a linear curve fit is applied to the responses presented above. This is done using a least squares polynomial fit of first order, which calculates the gradient as well as an offset. Although the measurement system was tared for each excitation location, a small offset can be seen in some cases. Thus, forcing the curve fit to pass through zero would alter the results. Using the gradients, a virtual set of loads $\mathbf{v}$ and responses $\boldsymbol{\mu}$ based on a force $F_z = 100.0N$ is calculated for the calibration. This allows to quantify the residuals more intuitively. Using equation (2.4), the calibration matrix $\boldsymbol{\beta}$ is calculated based on measurement series B0 to be

$$\boldsymbol{\beta} = \begin{bmatrix} -1.1579e4 & -5.2086e5 & -3.2768e3 \\ -1.1175e5 & +2.2044e2 & -2.3217e3 \\ -2.1251e3 & -3.0462e3 & +7.7824e4 \end{bmatrix}.$$

From the coefficients of matrix $\boldsymbol{\beta}$, it can be seen that the coefficients β_{12}, β_{21} and β_{33} are at least one order of magnitude larger than the remaining coefficients. This is a good indicator that the section load F_z is primarily influenced by the shear bridge, M_x by the bending bridge and M_y by the torsion bridge.

Using equation (2.5), the probable error p.e. is calculated as:

	Fz [N]	**Mx [Nm]**	**My [Nm]**
Probable errors	0.2212	0.4988	0.5211

Using equation (2.3), the loads can be reconstructed with the calibration matrix $\boldsymbol{\beta}$ from above. The residuals $\boldsymbol{\epsilon} = \mathbf{v}^{\text{calibration}} - \mathbf{v}^{\text{reconstructed}}$ are shown below:

Residual loads / excitation locations	**Fz [N]**	**Mx [Nm]**	**My [Nm]**
1	0.1426	0.06292	0.6500
2	0.1622	-0.2603	-0.6216
3	-0.1396	0.4567	0.6308
4	-0.4203	0.2934	0.6277
5	-0.2001	0.5902	-0.5863
6	0.3726	-0.9560	-0.2762
7	-0.0058	-0.6163	0.1567
8	0.0928	0.4229	-0.5850

Both the residuals and the probable error are very low. No significant improvement is observed for measurement series B1 with 12 load cases, neither for measurement series B2 with 20 load cases. All calibration matrices are similar and no clear trend is visible for the residual loads or the probable error. Thus, all following investigations are conducted based on measurement series B0.

4.3. Test Cases

The calibration can be tested by application of an unknown force at an unknown location. Based on a reading from the measurement system, the magnitude and location is reconstructed. The calibration was performed with single, nodal forces, but during flight, the aircraft will be subject to a more distributed load. Thus, testing the calibration with at least two simultaneous forces at different locations appears reasonable.

Note that the applied force locations are measured manually with a tape and that the strap has a width of 30.0 mm, leading to a precision of no more than 1.0 cm. Also note that the readings from the measurement system are taken visually and with a precision of three digits. Still, in all cases, the resulting force is reconstructed with a deviation of $\leq \pm 1.0N$ and the location with a deviation of $\leq \pm 2.0cm$.

Test Case 1: Two forces at the inner rib, center line and trailing edge

	Fz [N]	**X [m]**	**Y [m]**
Applied force	66.81	0.25	-1.01
Reconstructed	66.67	0.25	-1.03

Test Case 2: Two forces located diagonally on the wing, inner rib center line and outer rib trailing edge

	Fz [N]	X [m]	Y [m]
Applied force	66.81	0.25	-1.48
Reconstructed	67.03	0.26	-1.49

Test Case 3: Two forces located diagonally on the wing, inner rib leading edge, outer rib center line

	Fz [N]	X [m]	Y [m]
Applied force	66.81	-0.14	-1.74
Reconstructed	67.81	-0.13	-1.73

4.4. Temperature Influence and Means of Improvement

A significant temperature drift was observed during the measurements, especially for the bending bridge while the shear and torsion bridges showed smaller changes. In this context, two different effects need to be considered:

1. The overall temperature of the primary structure changes, e.g. as the aircraft gains altitude or the sun is heating the upper but not the lower side of the aircraft. These changes are expected to take place slowly and are acceptable, as the time periods of interest range from 10 to 30 seconds. Also, measuring (only) the dynamic increment with respect to a know condition, such as horizontal level flight, is acceptable for comparison with load simulation.
2. The surface temperature of the primary structure, incl. the strain gages mounted on the surface, changes. Possible sources could be cold air drafts or a change in solar radiation as the surface moves from the shadow into the sun or the angle of attitude changes, leading to a different projected area. These changes are expected to happen quickly and are less acceptable.

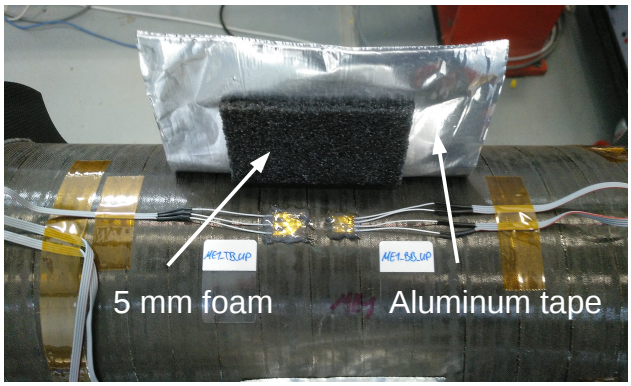

Figure 14: Example for covering the strain gages with silicone and an insulating cover

The area of the double linear strain bridge used for the bending bridge is approximately 30% smaller than the area of the +/-45° strain gages used for the shear and torsion bridge. Thus, their energy radiation capability is expected to be different. Using a contact-less infrared thermometer, the strain gage surface temperature was found to be very close to the surrounding temperature with a difference of no more than 1 or 2°C for all bridges. Thus, a different cooling gradient due to higher temperatures appears unfeasible.

In a next step, the laboratory door was opened, resulting in a drop of the surface temperature from 22°C to 17°C on the upper side of the tube and 15°C on the lower side. That spatial temperature difference is a likely explanation for the temperature drift described above.

Measuring the local temperature during flight would require a large number of sensors and a temperature compensation with the help of additional measurement equipment appear unfeasible. Instead, it was decided to add a cover to the strain gages. In a first step, a cover of 5 mm thick foam plus aluminum tape was added, see Figure 14. That cover should thermally insulate the strain gage, shield it against air drafts and the reflective aluminum tape should decrease the influence of solar radiation.

Different means were used to test the cover, including ice spray, a heat gun and a strong LED light. Application of the different means in a reproducible way is difficult, but the unprotected bridges react immediately to any disturbance, while the covered bridges take much longer to respond.

5. COMPARISON OF STRAINS FROM EXPERIMENT AND SIMULATION

5.1. Finite Element Model

To gain more confidence and to cross-check the measured results, a finite elements model (FEM) is

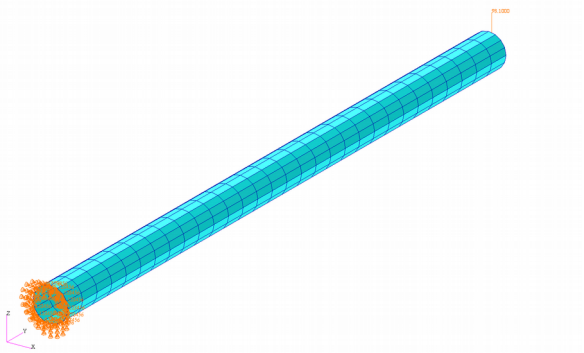

Figure 15: Finite elements model (FEM) of the main spar

helpful. A simple FE model is generated for MSC.Nastran, using the model generator ModGen [3] to set-up the shell elements and the remaining elements are added manually. The main spar is idealized using 16 shell elements in radial direction and 30 elements in span-wise direction, as shown in Figure 15. The wing root is clamped using single point constraints in all degrees of freedom and the load vector is introduced at the wing tip using a rigid body interpolation element. Note that this is only an idealized representation of the real structure, e.g. the ribs, the circular stiffening fibers (between the ribs and the tube) and the aluminum mounting are neglected. Also, the load introduction is different from the load distribution resulting from the attachment straps.

All plies of the carbon fiber laminate are modeled individually using PCOMP and MAT8 cards and the following stacking sequence: 90°, +20°, -20°, -20°, +20°, 90°. With a ply thickness of 0.145 mm, this leads to a total material thickness of 0.87 mm. The material characteristics of the unidirectional ply are given in Table 1.

E_1 $[Pa]$	E_2 $[Pa]$	G_{12} $[Pa]$	ν_{12}	t_{ply} $[mm]$
138.50e9	9.620e9	5.115e9	0.317	0.145

Table 1: Material characteristics of the unidirectional ply

5.2. Comparison of Strains

For the comparison, the two load cases are considered at their highest amplitude, leading to a load of $F_z = -98.1\ N$ and $F_z = -24.5N$ plus $M_y = -15.95Nm$ respectively. The strain and shear distribution is shown in Figure 16 for the first load case.

In a next step, the outer surface element strains are extracted from selected finite elements, which are close to the strain gages of section ME1 and ME2. Note that the strains are given for the center of each finite element and that the elements are only close to, but not exactly on the actual locations. Thus, small deviations resulting from the element sizes and locations can be expected. In the FE model, there are three effects which need to be compensated:

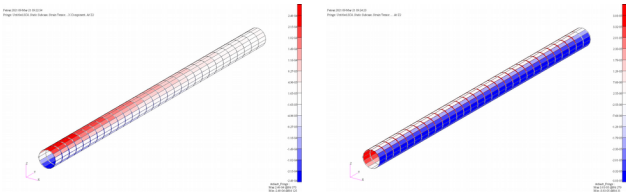

Figure 16: Strain (left) and shear (right) distribution for a loading at the outer rib, center line

1. Unlike in the measurement data, the element shear resulting from the shear and torsional load are not separated in the FE model. However, the shear extracted from the upper and lower side should be purely from torsional load and can be subtracted from the shear of the leading and trailing edge side.
2. There is a small angular error in the FE element shear because the corners of each element are exactly at 0°, 90°, 180° and 270° in radial direction, but the element centers are slightly off with the elements being tilted by +/-11.25°. This effect is compensated by adding the shear of the corresponding orthogonal element.
3. Unlike in the measurement data, the Nastran output for element shear is given as γ_{xy} with $\epsilon_{xy} = \gamma_{xy}/2$. The shear and torsion bridges measure ϵ_{xy}, thus this conversion must be accounted for.

In a last step, the measured bridge voltage U_{IN} needs to be translated to strains ϵ using

$$\epsilon = \frac{4 \cdot U_{IN}}{k \cdot N \cdot U_B} \tag{5.1}$$

with the strain gage factor $k = 2.09$ and the bridge number $N = 4$ for the bending, shear and torsion bridges. The results are shown in Tables 2 and 3 for the two load cases. It can be seen that the experiment and simulation match well. With a maximum difference of <8%, the shear bridge shows the largest difference.

Strain/Shear	**Bending**	**Shear**	**Torsion**
Experiment	1.86E-04	-2.23E-05	3.45E-06
Simulation	1.86E-04	-2.08E-05	-9.15E-11
Exp / Sim	99.94%	106.93%	-

Table 2: Comparison of experimental and simulated strains, loading at the outer rib, center line

Strain/Shear	**Bending**	**Shear**	**Torsion**
Experiment	4.57E-05	-5.62E-06	2.09E-05
Simulation	4.63E-05	-5.20E-06	1.96E-05
Exp / Sim	98.63%	107.97%	106.62%

Table 3: Comparison of experimental and simulated strains, loading at the outer rib, trailing edge

6. CONCLUSIONS AND OUTLOOK

This pre-test helped to familiarize with and gain confidence in the procedures involved for a successful strain gage calibration for in-flight loads measurements of a high altitude platform. The

concept that was developed theoretically in section 3.3 has proven to be suitable. The research questions formulated in section 1 are answered in the following.

As described in section 4.1, the three bending, shear and torsion bridges respond as expected and their relationships can be decoupled easily by the application of forces at different locations. Thus, the selected set-up appears suitable.

For this pre-test, the smallest number of excitation locations (eight locations) of measurement series B0 were sufficient to calculate the calibration matrix, see section 4.2. Five discrete masses (11 measurement samples) appear sufficient to establish the linear gradients.

The reconstruction of the applied loads in section 4.3 was possible with a deviation of $\leq \pm 1.0N$ and for the location with a deviation of $\leq \pm 2.0cm$.

The silicon coating combined with a cover with 5 mm foam plus aluminum tape provides an improved thermal insulation for the strain gages against surface temperature fluctuations as shown in section 4.4. The cover is very light-weight in terms of mass and influence on the aircraft primary structure. To increase the confidence in the measurements, two temperature sensor could be added below the covers, one on the upper and one lower side.

Using a simplified FE model, the strains could be predicted within the range of $\leq \pm 8\%$ as demonstrated in section 5.2. However, extracting the strains from the FE models was found more difficult than expected and involved a couple additional steps to compensate the “FE strain bridges” and create comparable the results.

Future work includes a test of the in-flight measurement equipment developed specifically for HAP. How well does it perform in comparison to a laboratory measurement system? More practical questions include thinking about a support of the aircraft with only one wing loaded and possible attachment points for loads when the outer skin is already installed.

REFERENCES

[1] Eckstrom, “Flight loads measurements obtained from calibrated strain-gage bridges mounted externally on the skin of a low-aspect-ratio wing,” NASA Langley Research Center, Hampton, VA, United States, Technical Report NASA-TN-D-8349, Dec. 1976, https://ntrs.nasa.gov/citations/19770009075.

[2] Jenkins, and DeAngelis, “A Summary of Numerous Strain-Gage Load Calibrations on Aircraft Wings and Tails in a Technological Format,” NASA Dryden Flight Research Center, Edwards, CA United States, Technical Memorandum NASA-TM-4804, Jul. 1997, https://ntrs.nasa.gov/citations/19970025651.

[3] Klimmek, T., “Parameterization of topology and geometry for the multidisciplinary optimization of wing structures,” in *CEAS 2009 - European Air and Space Conference*, Manchester, United Kingdom, 2009.

[4] Preisighe Viana, M. V., “Sensor calibration for calculation of loads on a flexible aircraft,” in *16th International Forum on Aeroelasticity and Structural Dynamics*, Saint Petersburg, Russia, 2015, http://elib.dlr.de/97681/.

[5] Schmücker, M., “Calibration of Main Components of an Aircraft for Loads,” FTI Engineering Network GmbH, Technical Report FV62 200-02, Feb. 2010.

[6] Sinske, J., Govers, Y., Handojo, V., and Krüger, W. R., “HALO Flugtest mit instrumentierten Aussenlasten fuer Aeroelastik- und Lastmessungen im DLR Projekt iLOADS,” in *Deutscher Luft- und Raumfahrtkongress*, Braunschweig, 2016.

[7] Skopinski, T. H., Aiken, W. S., and Huston, W. B., “Calibration of strain-gage installations in aircraft structures for the measurement of flight loads,” National Advisory Committee for Aeronautics. Langley Aeronautical Lab, Langley Field, VA, Technical Report NACA-TR-1178, Jan. 1954, http://ntrs.nasa.gov/search.jsp?R=19930090978.

[8] Voß, A., Handojo, V., Weiser, C., and Niemann, S., “Preparation of Loads and Aeroelastic Analyses of a High Altitude, Long Endurance, Solar Electric Aircraft,” presented at the AEC2020 Aerospace Europe Conference, Bordeaux, France, 2020, https://elib.dlr.de/133496/.

[9] Voß, A., Handojo, V., Weiser, C., and Niemann, S., “Results from Loads and Aeroelastic Analyses of a High Altitude, Long Endurance, Solar Electric Aircraft,” *Journal of Aeroelasticity and Structural Dynamics*, submitted.

[10] Voß, A., and Ohme, P., “Dynamic maneuver loads calculations for a sailplane and comparison with flight test,” *CEAS Aeronautical Journal*, vol. 9, no. 3, pp. 445–460, Apr. 2018, https://doi.org/10.1007/s13272-018-0300-9.

[11] “DLR - Flugexperimente - Dassault Falcon 2000LX.” [Online]. Available: https://www.dlr.de/fb/desktopdefault.aspx/tabid-3707/5786_read-70061/. [Accessed: 13-Jul-2021].

[12] “imc CRONOSflex.” [Online]. Available: https://www.imc-tm.com/products/daq-systems/imc-cronosflex/base-units/. [Accessed: 13-Jul-2021].